STEM Characterization of Dislocation Loops in Irradiated FCC Alloys

Pengyuan Xiu[a], Hongbin Bei[b], Yanwen Zhang[b,c], Lumin Wang[a,d], and Kevin G. Field[a]*

[a] Department of Nuclear Engineering and Radiological Sciences, University of Michigan, Ann Arbor, Michigan 48109, USA
[b] Materials Science and Technology Division, Oak Ridge National Laboratory, Oak Ridge, TN, 37831, USA
[c] Department of Materials Science and Engineering, University of Tennessee, Knoxville, TN, 37996, USA
[d] Department of Materials Science Engineering, University of Michigan, Ann Arbor, Michigan 48109, USA

Abstract

In this study, we demonstrate the methodology systematically developed for dislocation loop (perfect and faulted loops) imaging and analysis in irradiated face-centered-cubic (FCC) alloys using scanning transmission electron microscopy (STEM). On-zone [001] STEM imaging was identified as the preferred choice based on the comparison to (i) on-zone STEM imaging using other major low-index zone axes, (ii) two-beam bright field imaging condition near the [001] zone axis using conventional TEM (CTEM), and (iii) Rel-Rod CTEM dark-field (DF) imaging near the [011] zone axis. The effect of STEM collection angle on the contrast formation of dislocation loops was also investigated. The developed method was confirmed by imaging all populations of perfect and faulted loops of types a/2⟨110⟩{110} and a/3⟨111⟩{111} found in an ion irradiated $Ni_{40}Fe_{40}Cr_{20}$ alloy. The proposed STEM-based technique can easily identify said loops with a size greater than 10 nm without any assumptions such as those commonly made using the conventional Rel-Rod CTEM-DF technique. The recommended methodology in this study is developed as a quick and convenient tool that can be generally applied to irradiated FCC-based materials due to their common crystallography.

Keywords: Radiation effects; STEM characterization; dislocation loops; microstructure characterization; face-centered-cubic (FCC) alloy; Ni-based concentrated solid solution alloy; dislocation loop morphology

*Corresponding author: kgfield@umich.edu, University of Michigan, Ph: 734-764-4260

1. Introduction

Face-centered-cubic (FCC) based materials are attracting attention for potential use in advanced reactor applications due to their acceptable radiation resistance, corrosion resistance, ductility, and high temperature creep strength. Among all the observed radiation-induced microstructural changes, dislocation loops are of specific importance as they are known to contribute to the degradation of mechanical properties of FCC alloys [1–3]. The change in mechanical properties is primarily evaluated via hardening and embrittlement, where radiation-induced dislocation loops acting as obstacles for dislocation motion contribute to this response [4–6]. Perfect dislocation loops of type a/2 〈110〉 {110} and faulted dislocation loops of type a/3 〈111〉 {111}, where *a* represents the lattice parameter of the FCC crystal, are well known to form either under neutron, ion, or electron irradiation, or by quenching, in various FCC-based materials including silver [7,8], aluminum [9–13], gold [9], copper [7,8,14,15], austenitic steel [16–22], Ni or Ni-based superalloys [23–37], and Ni-containing multi-component solid solution alloys [38–44]. In general, perfect loops are considered mobile due to its Burgers vector being in-plane with the 〈110〉 close packed direction, while faulted loops are considered sessile [45,46]. Therefore, faulted loops are believed to contribute more to radiation hardening as compared to perfect loops [5,43]. This difference in the contribution to radiation hardening leads to studies on how to tailor an FCC material's response to irradiation, including the formation and evolution of these two types of dislocation loops using alloy design.

However, there has not yet been a convenient and standardized way to characterize and differentiate *both* a/2⟨110⟩{110} perfect and a/3⟨111⟩{111} faulted dislocation loops in irradiated FCC-based materials that has been widely used by the nuclear materials community. For example, conventional Rel-Rod TEM dark-field (CTEM-DF) imaging at **g**(311) near the [011] zone has been extensively used to image faulted dislocation loops [47,48] because of the white-on-black contrast formation exhibited when faulted loops are slightly inclined from the edge-on position. This method, however, is not suited to image perfect loops which do not consist of faulted planes. In addition, only two out of four variants of edge-on faulted loops can be captured in the DF images from using a TEM foil near [011] zone. When it comes to the loop density counting, it is common to use the assumption that the fraction of all four variants, [111] $[11\bar{1}]$ $[1\bar{1}1]$ $[\bar{1}11]$, of faulted loops are equal resulting in a simple multiplication factor to obtain the total density (e.g. both visible edge-on and non-visible, non-edge-on) of faulted loops. However, deviation from this assumption, e.g. observation of loop Burgers vector anisotropy, has been experientially observed in electron, neutron, and ion irradiated austenitic stainless steels with either internally generated stress field or when an external stress is applied [49]. Therefore, the simple assumption made in the Rel-Rod method may result in additional errors for the loop counting statistics for faulted loops while also generally negating the contributions of perfect loops to the microstructure. The result is the possibility of a skewed analysis used in subsequent alloy design, use, and performance considerations.

Another common method deployed for both FCC and body-centered cubic (BCC) alloys is the use of kinematic two-beam conditions bright field (BF) imaging in CTEM, where the ***g***-vector is selected and excited by carefully tilting to bring varying loops of a given Burgers vector in and out of contrast via the ***g•b*** invisibility criterion [50]. The CTEM-based method can become tedious because sequential series of sample tilting involving at least three or more ***g***-vectors are required to unambiguously determine the dislocation loop Burgers vectors and habit planes for both loop types. In addition, the deviation parameter, $\boldsymbol{s_g}$ needs to be kept slightly positive for all ***g*** vectors in order to keep the kinematic two-beam imaging condition [50]. The result is a complex experiment ripe for errors even when completed carefully and in detail. In addition, the resulting two-beam condition images still contain significant background contrast including thickness fringes and bend contours that can skew the interpretation and analysis of the loop type and size.

Yao et al. [51]**Error! Reference source not found.** looked to alleviate some of the inherent errors using CTEM by publishing a systematic work on projected dislocation loop morphologies using CTEM in irradiated BCC ferritic-based alloys. Within their work, the projected dislocation loop morphologies taken at a given kinematic two-beam condition can be used to infer the Burgers vector and habit plane. The work of Yao et al. was extended by Parish et al. [52] and Nathaniel et al. [53] where the projected dislocation loop morphologies are used in conjunction with scanning transmission electron microscopy (STEM) to provide rapid imaging and identification of loops with different Burgers vectors in BCC ferritic-based alloys. The culmination of these studies has led to wide-spread adoption of the STEM-BF method for dislocation loop imaging because of (i) the suppression of bend contour induced contrast and improved signal-to-noise ratio compared to CTEM-BF [54], (ii) the ability to exhibit all dislocation and dislocation loop structures in the thin foil without necessity to make simplifying assumptions **Error! Reference source not found.**, (iii) the handiness and reliability of identifying loop type from the loop morphology with the appropriate selection of zone axis [51], and (iv) the applicability of CTEM $\boldsymbol{g}\bullet\boldsymbol{b}$ and $\boldsymbol{g}\bullet\boldsymbol{R}$ criteria for dislocation and stacking fault analysis respectively in STEM [56]. To date, the above-mentioned advantages of STEM have been demonstrated almost exclusively for BCC ferritic-based alloys with no treatment for imaging faulted loops due to the expected high stacking fault energy [57] in ferritic alloys.

In the current study, the methodology of using on-zone STEM-BF for dislocation loop imaging is extended to irradiated FCC-based materials, with the goal of developing a standardized way to characterize and identify populations of perfect and faulted dislocation loops in a single micrograph that are both known to form in FCC-based materials upon irradiation. A nickel-based single-phase concentrated solid solution alloy (SP-CSA) $Ni_{40}Fe_{40}Cr_{20}$, which has an FCC crystal structure and a stacking fault energy in the realm where both perfect and faulted loops are anticipated under the chosen radiation condition, was used for this purpose. SP-CSAs are attracting more attentions in recent years due to their excellent void swelling resistance under irradiation [26,27,42,58–62], with only a handful of studies focused on dislocation loop evolution in this class of materials [26,39,43]. In the current study, various techniques in loop imaging using S/TEM have been systematically investigated including: the selection of the optimal zone axis, collection angle effects (BF vs. annular dark field - ADF), and the comparison between CTEM and STEM.

2. Experimental

2.1 Materials Synthesis, Ion Irradiation and S/TEM Sample Preparation

An FCC Ni-based SP-CSA, $Ni_{40}Fe_{40}Cr_{20}$ alloy, was used as the model alloy for the dislocation loop imaging after 3 MeV Ni^{2+} self-ion irradiation [63] to a peak damage level of 7.2 dpa at 500°C with a dose rate of 1.7×10^{-2} dpa/s predicted by the Stopping and Range of Ions in Matter (SRIM) 2013 code in "Detailed Calculation with Full Damage Cascades" mode [64–66]. The irradiation conditions centered the damage peak around 900 nm from the implantation surface. The $Ni_{40}Fe_{40}Cr_{20}$ alloy was chosen for reasons of (i) its unirradiated microstructure that is free of defect sinks such as pre-existing dislocations or precipitates; and (ii) the co-existence of $a/2\langle110\rangle\{110\}$ perfect and $a/3\langle111\rangle\{111\}$ faulted dislocation loops in the irradiated microstructure with the selected irradiation condition, which is a result of the sluggish loop evolution in this ternary alloy with relatively lower stacking fault energy compared to the chemically less complex binary alloy, Ni-20Fe [43]. The unirradiated microstructure of the $Ni_{40}Fe_{40}Cr_{20}$ alloy in this study is provided in Figure S1 in the Supplementary Information for reference. In other words, the combination of the $Ni_{40}Fe_{40}Cr_{20}$ ternary alloy and the radiation condition makes it ideal for the purpose of studying dislocation loop morphologies and loop type identification using S/TEM imaging. Detailed material synthesis and ion radiation parameters are provided elsewhere [43].

Following the ion irradiation, the electron backscatter diffraction (EBSD) microscopy technique coupled with a dual-beam Scanning Electron Microscope/Focused Ion Beam (SEM/FIB) was used to determine the crystal orientations of S/TEM thin foils ([001], [011] and $[\bar{1}11]$ in this study) prepared using the "lift-out" technique by FIB. The "flash polishing" technique [67] involving 0.05s ~ 0.12s electro-polishing using the reagent of 96% ethanol and 4% perchloric acid was then conducted to remove any FIB-induced damage to improve the overall imaging quality in S/TEM.

2.2 S/TEM characterization

All S/TEM characterization work on imaging dislocation loops in the irradiated $Ni_{40}Fe_{40}Cr_{20}$ sample was conducted at MC^2 using a Thermo Fisher Talos F200X G2 in STEM or TEM mode operating at 200 kV. Region of interests were selected to include most of the irradiated region within the lift-outs (100 ~ 1200 nm in depth range and 1100 nm in width) regardless of imaging conditions used.

2.2.1 On-Zone STEM-BF and STEM-ADF Imaging

The FEI Talos in STEM mode includes multiple STEM detectors (up to four) that allows for simultaneous collection of on-zone STEM Bright Field (STEM-BF), Annular Dark Field (STEM-ADF), and High Angle Annular Dark Field (STEM-HAADF) images. These imaging modes were used to characterize dislocation loops at the three major low-index zone axes: [001], [011], and $[\bar{1}11]$. Only these three major commonly used low-index zone axes were selected, though in practice the prescribed methodologies could be extended to other imaging orientations. A manufacturer indicated camera length (CL) of 98 mm coinciding with a collection angle of 0-8 mrad was the primary imaging configuration used within. STEM-BF images taken under these zone axes were compared with the simulated loop morphology maps, discussed in detail below, to investigate the optimal choice of zone axis for the purpose of identifying dislocation loop types. Here, *family* denotes if a loop is perfect or faulted, *type* denotes the specific Burgers vector and habit plane of dislocation loops, while *nature* denotes if they are comprised of vacancies or interstitials. The nature of the dislocation loops was not within the scope of this study.

Collection angle effects while imaging down the [001] zone axis were also investigated by simply changing the manufacturer indicated CL from 98 mm to 330 mm in STEM-BF and STEM-ADF imaging modes, coinciding with a collection angle of 0-8 and 0-3 mrad in STEM-BF mode and 22-52 and 7-16 mrad in STEM-ADF mode, respectively. STEM-BF and STEM-ADF images at CL of 98 mm were acquired as duplets, allowing for the exact region of interest to be compared between the different image generation configurations.

All STEM images were collected with 4096 × 4096 pixels with generic post-processing conducted to optimize the brightness and contrast of the images. Image dwell times were optimized to increase signal-to-noise ratios while minimizing drift within the captured images.

2.2.2 CTEM Imaging Techniques

In order to compare CTEM imaging to STEM-BF imaging, two common CTEM techniques to image dislocation loops were employed: (i) the kinematical two-beam conditions (deviation parameter $\boldsymbol{s_g} > 0$) in Bright Field (CTEM-BF) using $\boldsymbol{g}$ vectors of (020), $(\bar{2}20)$, $(\bar{2}00)$ and $(\bar{2}\bar{2}0)$ near [001] zone axis, and (ii) the Rel-Rod method in Dark Field (CTEM-DF) using $\boldsymbol{g}$ vectors of $(\bar{3}1\bar{1})$ and $(31\bar{1})$ near [011] zone axis to image two edge-on variants (out of total four variants) of faulted loops. The CTEM imaging results are compared with the STEM-BF images taken at the same area of the thin foil.

3. Results and Discussions

3.1 On-Zone STEM-BF Imaging

Figure 1 is an illustration of a dislocation loop lying on its habit plane within the S/TEM, and how Bragg diffraction contrast or the strain field near a dislocation loop core is projected onto the projection viewing plane (i.e. onto the CCD capture device), where the electron traveling direction is normal to the projection viewing plane. Note, Figure 1 is an adaption from Yao et al [51]. The projection angle, θ, which denotes the angle between the habit plane and the projection plane can range from 0° to 90°. If the dislocation loop core is circular in nature, the major to minor axis length ratio (aspect ratio) for the projected ellipse is 1:cos(θ). If θ is 0°, the habit plane and the projection plane are the same and the aspect ratio is 1:1, allowing for direct visualization of the dislocation loop shape (e.g. circular or faceted). This specific imaging contrast is typically referred to as plane-view loops. If θ is 90°, the habit plane and the projection plane are normal, and thus only the side or edge of the dislocation loops will be visible generating loop contrast denoted as edge-on. Note the Burgers vector of the dislocation loop in Figure 1 is assumed to be normal to the habit plane.

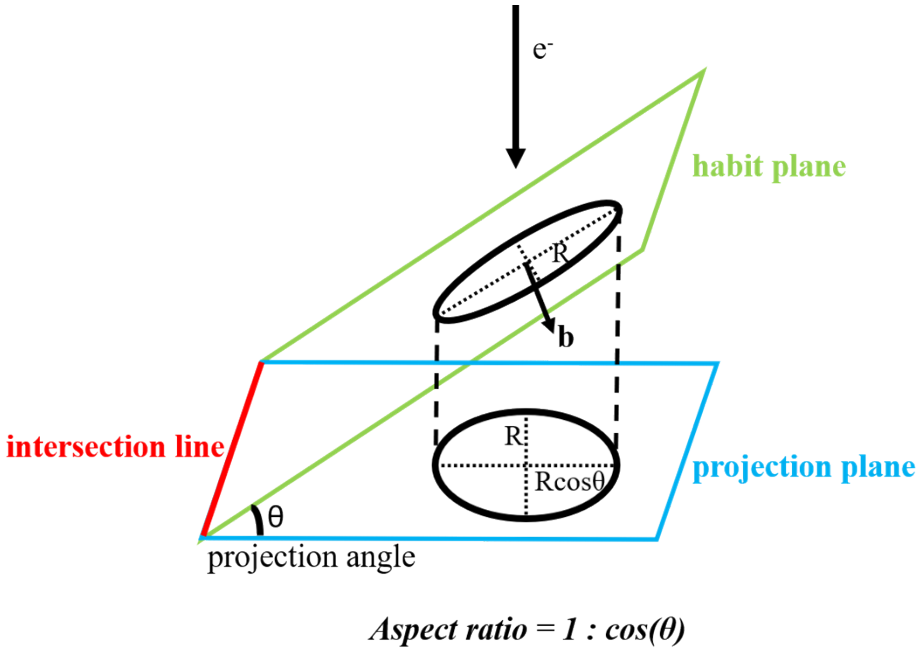

Figure 1. The schematic of an assumed circular-shape dislocation loop lying on an inclined habit plane being imaged in TEM with electrons traveling down the optic axis, and the resultant image formed on the projection viewing plane. The aspect ratio of the elliptical loop in the S/TEM image is a function of the projection angle, θ. Adapted from Ref. [51].

Based on the schematic in Figure 1, the dislocation loop aspect ratio, and thus projected morphology, can be determined if the habit plane and projection angle are known. As discussed, in FCC materials it is commonly accepted that perfect loops form with a Burgers vector and habit plane of a/2⟨110⟩{110} and faulted loops form with a Burgers vector and habit plane of a/3⟨111⟩{111}. Tables 1-3 summarizes the crystallographic information of habit planes and Burgers vectors of all loop variants assuming an FCC crystal structure such as that present for the $Ni_{40}Fe_{40}Cr_{20}$ alloy when imaged using on-zone STEM-BF on the [001], [011] and the $[\bar{1}11]$ zone axis respectively. The projection angle and the resultant aspect ratio of the ellipses are calculated and shown, together with the line direction of the intersection between the dislocation loop habit plane and the foil plane. Multiple low-index ***g*** vectors near each zone axis and the ***g•b*** values for the invisibility criterion are provided as well.

Table 1. Crystallographic information between dislocation loop habit planes and (001) *viewing plane imaged under* [001] *zone axis.*

Habit Plane*	(111)	$(\bar{1}11)$	$(1\bar{1}1)$	$(\bar{1}\bar{1}1)$	(110)	$(1\bar{1}0)$	(011)	$(0\bar{1}1)$	(101)	$(\bar{1}01)$
Family	faulted	faulted	faulted	faulted	perfect	perfect	perfect	perfect	perfect	perfect
Burgers vector, ***b****	a/3[111]	a/3$[\bar{1}11]$	a/3$[1\bar{1}1]$	a/3$[\bar{1}\bar{1}1]$	a/2[110]	a/2$[1\bar{1}0]$	a/2[011]	a/2$[0\bar{1}1]$	a/2[101]	a/2$[\bar{1}01]$
Projection angle, θ	54.74°	54.74°	54.74°	54.74°	90°	90°	45°	45°	45°	45°
Aspect ratio, cos θ	1:0.577	1:0.577	1:0.577	1:0.577	edge-on	edge-on	1:0.707	1:0.707	1:0.707	1:0.707
Direction of intersection line between loop plane and foil plane	$[1\bar{1}0]$	[110]	[110]	$[1\bar{1}0]$	$[1\bar{1}0]$	[110]	[100]	[100]	[010]	[010]
$\boldsymbol{g}_{020}\bullet\boldsymbol{b}$	nonzero	nonzero	nonzero	nonzero	nonzero	nonzero	nonzero	nonzero	0	0
$\boldsymbol{g}_{\bar{2}20}\bullet\boldsymbol{b}$	0	nonzero	nonzero	0	0	nonzero	nonzero	nonzero	nonzero	nonzero
$\boldsymbol{g}_{\bar{2}00}\bullet\boldsymbol{b}$	nonzero	nonzero	nonzero	nonzero	nonzero	nonzero	0	0	nonzero	nonzero
$\boldsymbol{g}_{\bar{2}\bar{2}0}\bullet\boldsymbol{b}$	nonzero	0	0	nonzero	nonzero	0	nonzero	nonzero	nonzero	nonzero

*Burgers vector ***b*** variant for dislocation loops is chosen so that its angle with electron beam direction (in this case, [001]), or the projection angle θ, is always non-blunt (between 0° and 90°). For example, a/3[111] with angle of 54.74° is chosen over a/3$[\bar{1}\bar{1}\bar{1}]$ with angle of 125.26° at [001] zone axis.

Table 2. Crystallographic information between dislocation loop habit planes and (011) *viewing plane imaged under* [011] *zone axis.*

Habit Plane	(111)	$(\bar{1}11)$	$(1\bar{1}1)$	$(11\bar{1})$	(110)	$(\bar{1}10)$	(011)	$(01\bar{1})$	(101)	$(\bar{1}01)$
Family	faulted	faulted	faulted	faulted	perfect	perfect	perfect	perfect	perfect	perfect
Burgers vector, ***b***	a/3[111]	a/3$[\bar{1}11]$	a/3$[1\bar{1}1]$	a/3$[11\bar{1}]$	a/2[110]	a/2$[\bar{1}10]$	a/2[011]	a/2$[01\bar{1}]$	a/2[101]	a/2$[\bar{1}01]$
Projection angle, θ	35.26°	35.26°	90°	90°	60°	60°	0°	90°	60°	60°
Aspect ratio, cos θ	1:0.816	1:0.816	edge-on	edge-on	1:0.5	1:0.5	1:1	edge-on	1:0.5	1:0.5
Direction of intersection line between loop plane and foil plane	$[01\bar{1}]$	$[01\bar{1}]$	$[21\bar{1}]$	$[2\bar{1}1]$	$[1\bar{1}1]$	$[11\bar{1}]$	N/A	[100]	$[11\bar{1}]$	$[1\bar{1}1]$
$\boldsymbol{g}_{\bar{1}1\bar{1}}\bullet\boldsymbol{b}$	nonzero	nonzero	nonzero	nonzero	0	nonzero	0	nonzero	nonzero	0
$\boldsymbol{g}_{\bar{2}00}\bullet\boldsymbol{b}$	nonzero	nonzero	nonzero	nonzero	nonzero	nonzero	0	0	nonzero	nonzero
$\boldsymbol{g}_{02\bar{2}}\bullet\boldsymbol{b}$	0	0	nonzero	nonzero	nonzero	nonzero	0	nonzero	nonzero	nonzero
$\boldsymbol{g}_{11\bar{1}}\bullet\boldsymbol{b}$	nonzero	nonzero	nonzero	nonzero	nonzero	0	0	nonzero	0	nonzero

Table 3. Crystallographic information between dislocation loop habit planes and $(\bar{1}11)$ *viewing plane imaged under* $[\bar{1}11]$ *zone axis.*

Habit Plane	(111)	$(\bar{1}\bar{1}1)$	$(\bar{1}1\bar{1})$	$(\bar{1}11)$	(110)	$(\bar{1}10)$	(011)	$(01\bar{1})$	(101)	$(\bar{1}01)$
Family	faulted	faulted	faulted	faulted	perfect	perfect	perfect	perfect	perfect	perfect
Burgers vector, ***b***	a/3[111]	a/3$[\bar{1}\bar{1}1]$	a/3$[\bar{1}1\bar{1}]$	a/3$[\bar{1}11]$	a/2[110]	a/2$[\bar{1}10]$	a/2[011]	a/2$[01\bar{1}]$	a/2[101]	a/2$[\bar{1}01]$
Projection angle, θ	70.53°	70.53°	70.53°	0°	90°	35.26°	35.26°	90°	90°	35.26°
Aspect ratio, cos θ	1:0.333	1:0.333	1:0.333	1:1	edge-on	1:0.817	1:0.817	edge-on	edge-on	1:0.817
Direction of intersection line between loop plane and foil plane	$[01\bar{1}]$	[101]	[110]	N/A	$[1\bar{1}2]$	[110]	$[01\bar{1}]$	[211]	$[12\bar{1}]$	[101]
$\boldsymbol{g}_{\bar{2}\bar{2}0}\bullet\boldsymbol{b}$	nonzero	nonzero	0	0	nonzero	0	nonzero	nonzero	nonzero	nonzero

$\boldsymbol{g}_{\bar{2}0\bar{2}}\bullet\boldsymbol{b}$	nonzero	0	nonzero	0	nonzero	nonzero	nonzero	nonzero	nonzero	0
$\boldsymbol{g}_{02\bar{2}}\bullet\boldsymbol{b}$	0	nonzero	nonzero	0	nonzero	nonzero	0	nonzero	nonzero	nonzero

Inclined faulted loops and stacking faults are known to exhibit repetitious white-black contrast within the perimeter of the loop when imaged using CTEM two-beam conditions. In those cases, only one ***g*** vector is activated (be on the Ewald sphere in the reciprocal space) besides the transmitted beam, and therefore, only one phase factor change, $e^{i\theta}$ resulting in electron beam interference between the beam diffracted by the perfect crystal planes and the faulted crystal planes. This interference phenomenon leads to the typical black-white repeating fringe contrast for faulted loops when imaged using two-beam conditions. However, in the case in our study, because faults are imaged at an on-zone (low index) condition, all ***g***s in the imaging plane are activated, with at least a two-fold degree of symmetry. That means whenever there is an activated ***g*** that causes a phase factor of $e^{i\theta}$, there is a corresponding activated ***-g*** that causes a phase factor of $e^{-i\theta}$. For a faulted dislocation loop that is imaged using on-zone STEM, the imaging contrast is a result of the superimposition from multiple sets of dipoles of black-white and white-black contrast. A full dark shadow, or shadow contrast, ends up exhibiting the overall contrast of the faulted dislocation loop when imaged using on-zone STEM-BF. A comprehensive study that systematically demonstrates this with experimental and simulation work is in Ref. [68].

Stacking faults in FCC materials on an inclined plane (either a/3{111} or a/6{112}) when imaged using two-beam conditions is generally visible on an electron micrograph as a repeating pattern of parallel fringes running parallel to the intersection between the fault plane and the plane of the foil. The number of repetitions in the fringe pattern is dependent on the imaging conditions used [69,70] and stacking fault size. In the case of radiation-induced dislocation loops, the inserted fault plane is exclusively a/3{111} [67,71–73] and therefore, the intersection direction and thus theoretical fringes direction can be calculated, as provided in Tables 1-3. It is interesting to note that this direction is always along the ⟨110⟩ family of directions, for any inclined variants of faulted loops under any of the three selected low-index zone axes. Theoretical and experimental details on the formation of stacking fault contrast can be found elsewhere with great thoroughness [69,74].

Using the information presented in Tables 1-3, dislocation loop morphology maps at on-zone conditions were constructed and are shown in Figures 2-4 with the corresponding diffraction patterns for zone axes of [001], [011] and $[\bar{1}11]$, respectively. For the elliptical projection of the inclined dislocation loops in the thin foil, their major axis direction is aligned with the intersection line direction, as illustrated in Figure 1. In some cases, two different loop variants can give the same morphology on the projection plane. For example, the a/3(111) and a/3$(\bar{1}\bar{1}1)$ faulted loops in Figure 2 both exhibit elliptical shapes with the identical aspect ratio and the direction of the major axis. Therefore, it is advantageous to use the on-zone STEM method to rapidly determine the total loop density for each family of loop (i.e. perfect or faulted) by using a single on-zone tilting condition, while one is still advised to use the tedious but necessary multiple tilting series to determine the type of each dislocation loop, if needed.

Inclined faulted loop shadow contrast arises in the on-zone STEM imaging due to the ***g•R*** invisibility criterion [56,75], as there always exists some if not all excited ***g*** vectors such that ***g•R*** invisibility condition is not satisfied and the shadow contrast is visible. Thus, in most cases, loops showing shadow contrast are identified as faulted loops, and loops without interior shadow contrast are identified as perfect loops due to the lack of inserted faults. However, this rapid method for determining if a loop is faulted based on the observed shadow contrast fails when a faulted loop is in plane and normal to electron traveling direction, i.e., when the in plane a/3$[\bar{1}11]$($\bar{1}$11) faulted loop is imaged at the on-zone $[\bar{1}11]$ condition. In this case, all ***g*** vectors in the $(\bar{1}11)$ plane get excited, just like imaging conducted at other zone axes such as [001] and [011], but all the excited

g vectors satisfy the invisibility condition of ***g•R***=0 because ***R*** is normal to the faulted loop plane and thus to all excited ***g*** vectors. Therefore, the in-plane faulted loop morphology at the on-zone [$\bar{1}$11] condition was predicted to not exhibit the characteristic interior shadow contrast and is depicted as such in Figure 4.

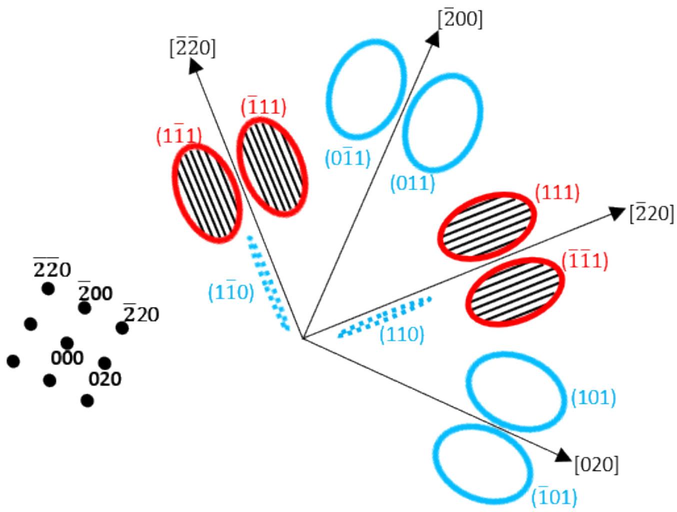

Figure 2. Simulated diffraction pattern and dislocation loop morphology map of FCC based alloys under [001] *zone axis without considering* ***g•b*** *invisibility criterion. Red loops with inside shadow contrast denote inclined faulted loops, blue elliptical loops without inside shadow contrast denote inclined perfect loops, dotted blue loops perimeters denote edge-on perfect loops. Pre-factors associated with the lattice parameter are omitted for visual clarity.*

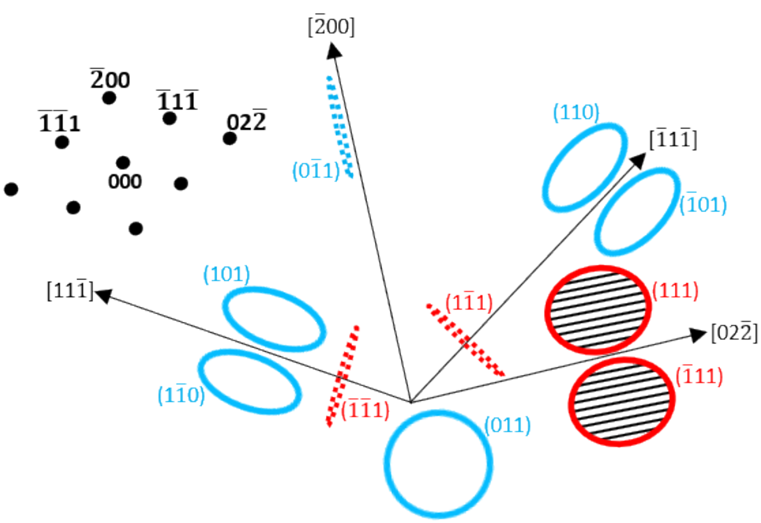

Figure 3. Simulated diffraction pattern and dislocation loop morphology map of FCC based alloys under [011] *zone axis without considering* ***g•b*** *invisibility criterion. Red loops with inside shadow*

contrast denote inclined faulted loops, blue loops without inside shadow contrast denote perfect loops, dotted loop perimeters of either color denote edge-on loops. Pre-factors associated with the lattice parameter are omitted for visual clarity.

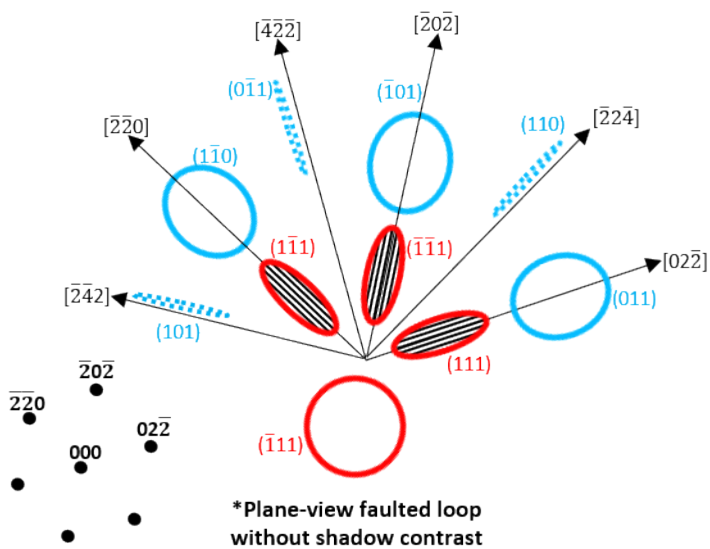

Figure 4. Simulated diffraction pattern and dislocation loop morphology map of FCC based alloys under $[\bar{1}11]$ *zone axis without considering **g•b** invisibility criterion. Red loops with inside shadow contrast denote inclined faulted loops, a red loop without inside shadow contrast denote in-plane plane-view faulted loop, blue loops without inside shadow contrast denote perfect loops, and dotted blue loop perimeters denote edge-on perfect loops. Pre-factors associated with the lattice parameter are omitted for visual clarity.*

In order to confirm the validity of the simulated loop morphology maps in Figures 2-4, cross-sectional on-zone STEM-BF images were acquired for the irradiated $Ni_{40}Fe_{40}Cr_{20}$ alloy under the three zone axes of [001], [011] and $[\bar{1}11]$ as shown in Figures 5-7, respectively. In all three images, the irradiation direction is from the top of the page, with the damage peak near 900 nm from the free surface based on ion range calculations [43]. The resulting irradiation damage variation from top to bottom of the image, image force from the free surface, and the interjected interstitial effect [76–79] are the primary driving factors for the variances in loop density and type as a function of distance from the free surfaces. Here, it is noted that both perfect and faulted loop types with varying sizes are formed under irradiation and observed in Figures 5-7.

On-zone [011] and on-zone $[\bar{1}11]$ STEM-BF images were taken at the same region of interest to demonstrate the disappearance of shadow contrast in faulted loops when transitioned from an inclined orientation in Figure 6 ([011] zone axis) to an in-plane orientation in Figure 7 ($[\bar{1}11]$ zone axis) as indicated by red circles in Figures 6 & 7. Figures 6 & 7 confirm the prediction from the simulated morphology maps where the in-plane loop type in the $[\bar{1}11]$ on-zone STEM image does not exhibit the shadow contrast while it does when imaged down the [011] zone axis.

The FIB lift outs prepared with EBSD for foils with [001] and [011] orientation make the tilting within STEM to be minimum, resulting in the improved image quality in Figures 5 & 6 with sharp dislocation loop core contrast and low noise level. The image quality in Figure 7 corresponding to on-zone $[\bar{1}11]$ STEM-BF, however, is reduced compared to Figure 5 and 6 due to the TEM foil being tilted from the nearly normal to the electron beam position on the [011] orientation to the highly inclined $[\bar{1}11]$ orientation. The large tilting angle, β, of ~35° between the two orientations corresponds to ~46% increase of effective thickness of the foil down the electron penetrating direction, resulting in quite significant beam broadening and spatial resolution reduction, shown in Figure 7, due to multiple electron scatterings in the sample with thickness greater than one electron mean-free-path [80]. The "black spots" also appear in Figure 6, and in Figure 7 with higher frequency, while they are not observed in Figure 5 where the effective thickness is the smallest among the three images. These small features are believed not to be caused by FIB damage, because of the flash polishing that has been conducted to effectively remove the surface damaged layer. These "black spots" features might be just modal contrast indicative of the local structure of the alloy, which arises when the effective thickness is increased. It is expected though, that the image quality should be significantly improved by reducing the apparent thickness effects from excessive sample tilting by preparing samples that are orientated near the exact $[\bar{1}11]$

zone axis. An example of such is provided in Figure S2 in the Supplementary Information where another on-zone [$\bar{1}$11] STEM-BF image is taken at a different sample area with reduced thickness showing improved image quality. Regardless, the variance in image quality between Figures 6 & 7 highlights a distinct advantage of STEM where thickness variations are less of an impact on the signal-to-noise collection compared to CTEM [50].

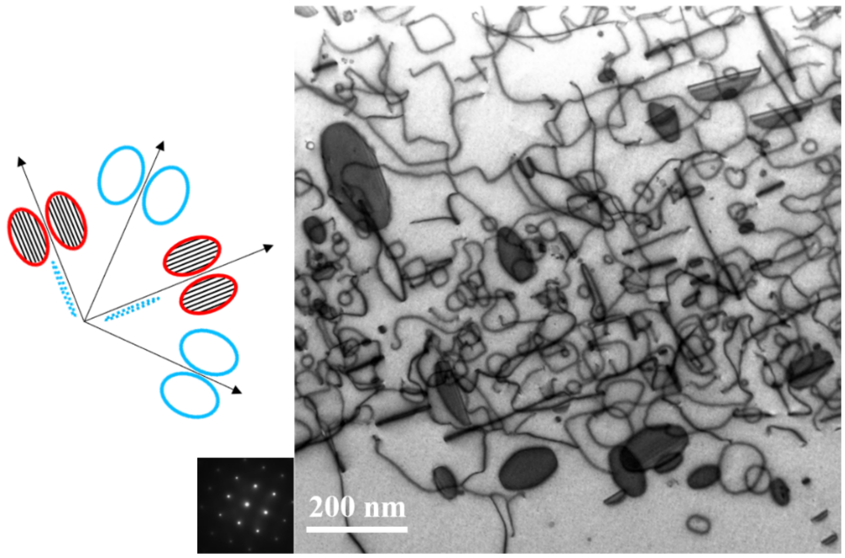

Figure 5. Cross-sectional on-zone [001] *STEM-BF image of irradiated* $Ni_{40}Fe_{40}Cr_{20}$ *with correctly oriented simulated morphology map and experimental diffraction pattern. For labelling of crystallographic directions, please refer to Figure 2.*

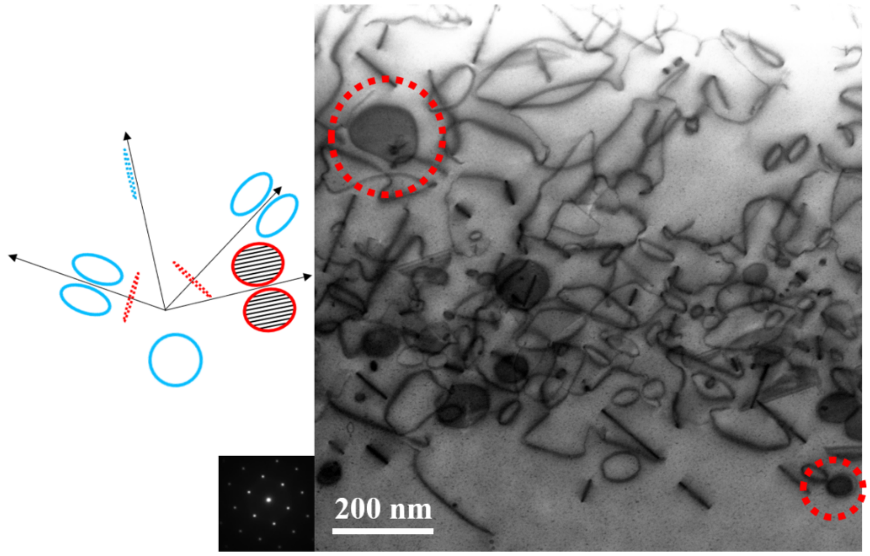

Figure 6. Cross-sectional on-zone [011] *STEM-BF image of irradiated* $Ni_{40}Fe_{40}Cr_{20}$ *with correctly oriented simulated morphology map and experimental diffraction pattern. For labelling of crystallographic directions, please refer to Figure 3. Note, that two inclined faulted loops showing shadow contrast are highlighted using red circles, while the contrast disappears in Figure 7 when these two loops are in-plane.*

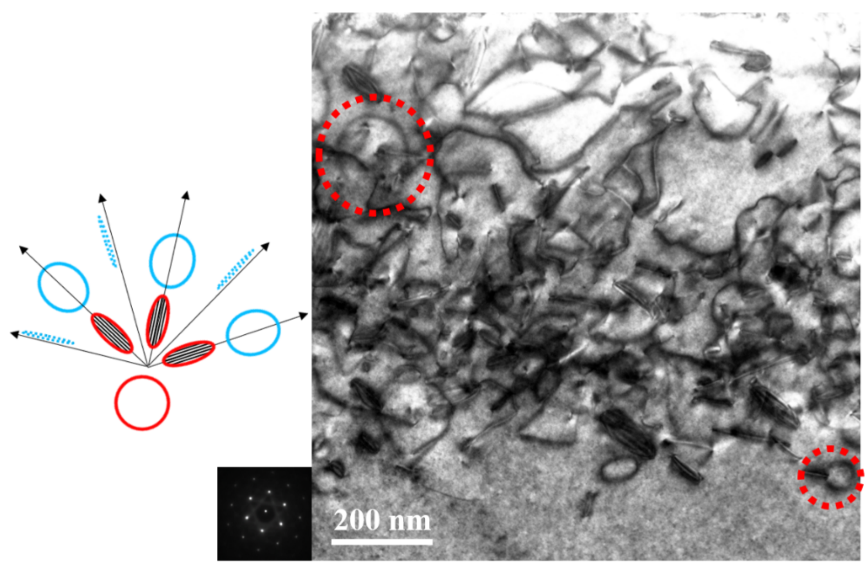

Figure 7. Cross-sectional on-zone $[\bar{1}11]$ *STEM-BF image of irradiated* $Ni_{40}Fe_{40}Cr_{20}$ *with correctly oriented simulated morphology map and experimental diffraction pattern. For labelling of crystallographic directions, please refer to Figure 4. Note, that in-plane faulted loops without shadow contrast are highlighted using red circles, while the contrast appears in Figure 6 when these two loops are inclined.*

It appears that faulted loop morphology in the simulated maps and STEM micrographs are very consistent, in terms of the aspect ratio and the major axis direction in the projected elliptical loops. For example, in Figure 5, the major axes of faulted loops projection under zone axis of [001] are along the $[\bar{2}20]$ and $[\bar{2}\bar{2}0]$ directions, which are normal to each other. Perfect experimental loops morphology in the STEM image, however, are not always exactly directly replicated via the simulated morphology maps. Some dislocation loops do not appear rounded, but rather, faceted in either hexagonal or rhombus shape, depending on the loop type and size [81] [46]. Some perfect loops open up to form entangled dislocation networks upon growth and interaction with other line dislocation or dislocation loops during irradiation [43] [82]. Both factors could contribute to non-elliptical projections from non-circular loop shape, which was initially assumed when the loop morphology map was constructed. Nevertheless, the STEM-BF technique still enables imaging of these complex morphologies. The edge-on perfect loops generally match the simulated and expected morphologies, indicating their habit plane is consistent with the simulated loop map. For example, in Figure 5, edge-on perfect loops lying on (110) and $(1\bar{1}0)$ habit planes are observed to match the simulated loop morphology map. This observation indicates that faulted loops tend to preserve the circular shape on their {111} habit plane during irradiation, resulting in their elliptical projection more rigidly satisfying the loop morphology maps in Figures 2-4. Perfect loops, on the other hand, present a higher degree of freedoms for their morphology, and some discrepancies are observed between the STEM images and the loop morphology maps.

In principle, all three low index zone axes allow one to image all dislocation loops in the on-zone STEM-BF mode with the aid of the corresponding rotation corrected diffraction pattern according to the morphology maps presented in Figures 2-4. However, due to the complications under certain imaging conditions discussed before, a preferred zone axis used for STEM-BF imaging can be suggested. The criteria of choosing the optimal zone axis to image dislocation loops should be aligned with: (i) relative ease to observe loop morphology, and (ii) straightforward differentiation of loop family (perfect vs. faulted) based on observed loop interior contrast and morphology. Based on those, it is highly desired that the choice of the zone axis would allow all faulted loops to be inclined to provide direct imaging of the shadow contrast, rather than some variants being either edge-on or in plane-view.

The loop morphology map of the [001] zone axis in Figure 2 shows that all four variants of faulted loops are non-edge-on with an aspect ratio of the projected ellipses of 1:0.577. They elongate along the $[\bar{2}\bar{2}0]$ and $[\bar{2}20]$ according to the diffraction pattern. The STEM-BF image in Figure 5 exhibits the matching of the faulted loop morphology, which makes it straightforward to identify and count with accuracy. The [011] zone axis is inferior compared to the [001] zone axis as shown in Figure 3, even though there are no plane-view faulted loops. There are two variants of edge-on faulted loops, $[1\bar{1}1]$ and $[\bar{1}\bar{1}1]$, which are 70.52° apart, together with one variant of edge-on perfect loops $[0\bar{1}1]$ having 35.26° with both edge-on loop variants. The identification of the loop types from the [011] STEM-BF image is still achievable with the aid of the rotation corrected diffraction pattern, but not as convenient or unambiguous in the case of [001] zone. Lastly the $[\bar{1}11]$ zone appears to be the least ideal choice. Shown in Figure 4 is the simulated loop morphology map of $[\bar{1}11]$. It is shown that the aspect ratio of the faulted loops is 1:0.33, which is quite close to edge-on loops in the image that could cause additional confusion and errors. Most importantly, one variant of plane-view faulted loops exists under this imaging condition, where they do not exhibit shadow contrast, and therefore causes additional confusion for its differentiation with inclined perfect loops. The result of the above analysis is the finding that

STEM-BF imaging down the [001] zone axis is suggested as the preferred orientation over any other low-index major zone axes.

It is noted that the proposed on-zone STEM-BF imaging technique for dislocation loop imaging heavily utilizes the observed loop morphology as well as the visibility of the shadow contrast from inclined faulted loops, both of which require loop size to be beyond a certain threshold so that one can determine these morphological features without ambiguity from the STEM micrographs. Here, the threshold was found near 10 nm. Although loops below this threshold cannot be unambiguously identified using the recommended techniques, these small dislocation loops are not typically considered as strong obstacles to dislocation motion [83], especially when their density is lower than the dislocation loops with greater size. The dislocation loop induced hardening and embrittlement under irradiation is a result of a balanced combination of density, size and barrier strength according to the dispersed barrier hardening model [84]. The weak barrier characteristics of these small dislocation loops [83] mean they contribute significantly less to radiation hardening compared to larger dislocation loops in irradiated FCC alloys. Therefore, the proposed methodology can provide insights on microstructure-property relationships whenever a significant population of dislocation loops above the given threshold are present within a given material. Under the circumstances where it is expected that small dislocation loops are of great significance to a study, it is recommended to use the two-beam conditions and Tables 1-3 for identifying loop types by examining the visibility of dislocation loops. It should be noted that the two-beam conditions can still be performed using the STEM-BF techniques which will reduce erroneous background contribution compared to CTEM techniques [56,68].

Based on the criteria above and discussion regarding Figures 2-4 and Figures 5-7, the choice of [001] zone STEM-BF imaging is suggested as the preferred orientation among all three studied zone axes, as it meets all desired criteria including the observation that all faulted loops can exhibit the shadow contrast in the STEM-BF image. Note that the recommendation must be taken at the discretion of the research, as different alloys, irradiation conditions, etc. could alter the morphology of the loops and thus our recommendations should not be taken blindly for vastly different conditional domains.

3.2 STEM (-BF and -ADF) Collection Angle Effects

Besides the specimen quality, which can include sample thickness discussed in Section 3.1 and FIB damage removal via flash-polishing, etc., there are multiple factors and conditions using a STEM microscope that can affect imaging contrast and quality as well. Here, we focus on commonly manipulated imaging conditions with the first being the alteration of manufacturer indicated CL and selection of STEM detector. Note that, alteration of the CL will change the projected angles onto the STEM detectors and thus alters the collection angle of the system. Figure 8 shows three on-zone [001] images: STEM-BF CL 98 mm, STEM-BF CL 330mm, and STEM-ADF CL 98mm with the collection angle of 0-8 mrad, 0-3 mrad, and 22-52 mrad respectively. Imaging collection conditions of pixel dwell time of 12.73 μs and pixel counts of 2048 by 2048 were kept identical between images in Figure 8. As can be seen, the image contrast and quality vary significantly when the collection angle is changed.

Intuitively from STEM-BF images in Figures 8(a) and (b), with decreasing CL and higher collection angle, the signal-to-noise ratio is significantly improved, and the shadowed diffraction contrast in faulted loops increases, because more signal counts including transmitted electrons and low angle diffracted electrons get collected by the bright-field detector. The signal level of STEM-ADF image in Figure 8(c) is significantly lower than the STEM-BF images as the ADF detector only captures portions of the diffracted beam. Meanwhile, more details are observed in the STEM-

ADF image, especially when there are features overlapping, indicating a better image resolution compared to the two STEM-BF images.

All these observations are confirmed by conducting line profiles across the long axis of perfect loops using ImageJ [85,86], with a representative line profile shown in Figure 8(d), where the signal counts in relative units is plotted as a function of the position of the scan. The full-width-half-max (FWHM) at the perfect loop core have been measured to be 10.95±1.98 nm, 13.39±3.96 nm and 6.91±1.93 nm, with the signal-to-noise ratio measured at the interior region ("featureless") of the loops to be 30, 16, and 3 (unitless, e.g. I/I_0) for the three profiles obtained from Figure 8(a), (b) and (c), respectively. The quantitative results verify that STEM-ADF indeed has the highest diffraction contrast resolution, while STEM-BF with a CL of 98 mm provides the best image quality in terms of the signal-to-noise ratio.

(a) (b)

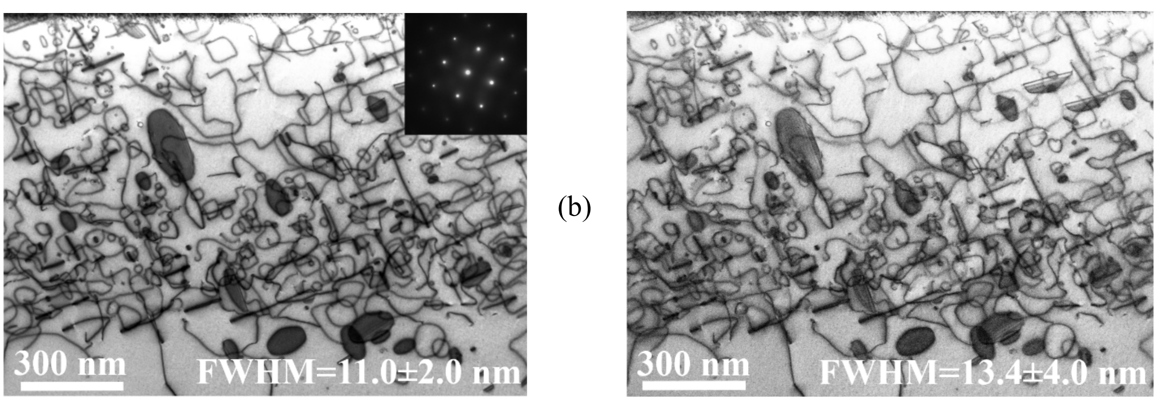

(c) 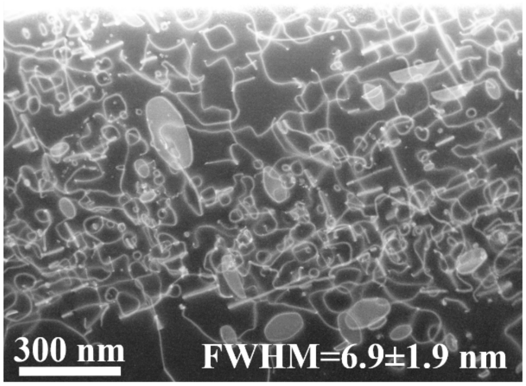

(d) 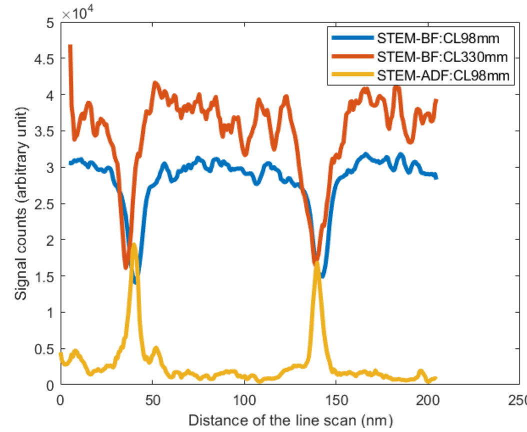

Figure 8. Same area of the on-zone [001] *at different conditions: (a) STEM-BF with CL of 98 mm, (b) STEM-BF with CL of 330 mm, and (c) STEM-ADF with CL of 98 mm. The collection angles are 0-8, 0-3, and 22-52 mrad, respectively. (d) Plot profile generated from a line across the long axis of an identical perfect loop in (a-c). The FWHM of perfect dislocation loop core in (d) is measured and labelled in (a), (b) and (c) respectively.*

Li et al. [87] and Anderson et al. [88] have evaluated the variances of quantification of microstructural features associated with hand labelling images, which can be 10-20% difference across researchers. Changes in loop size based on contrast resolution are minimum compared to other errors such as hand labelling and human interpretation of contrast. Therefore, although STEM-ADF provides better resolution, it will not significantly impact the overall error of the quantification technique used as human-based errors overwhelm the systematic experimental errors. For the purpose of dislocation loop imaging in the current study, STEM-BF with CL of 98 mm is sufficient, with the aid of STEM-ADF image to double check potential overlapping features. STEM, again, has a distinct advantage compared to CTEM as simultaneous acquisition of BF and ADF signals is routine with most modern STEM instruments. It is noted that all these conditions are affected by various factors including sample thickness, specimen surface quality, STEM accelerating voltage, and so on. The optimal combination of the STEM settings, therefore, may change depending on a given researcher's situations.

3.3 CTEM-BF Two-Beam Conditions Imaging

Figure 9 presents the on-zone [001] STEM-BF and the CTEM-BF kinematical two-beam condition images near the [001] zone axis using various ***g*** vectors of (020), $(\bar{2}20)$, $(\bar{2}00)$, and $(\bar{2}\bar{2}0)$ respectively, taken at the same sample area to correlate and compare. As can be seen, the traditional loop Burgers vector analysis using CTEM two-beam conditions based on the invisibility criterion is consistent with the on-zone STEM-BF imaging, where consistency across these two methods validates the feasibility of the proposed on-zone STEM method.

The advantage of the STEM method is demonstrated in Figure 9a, where all dislocation loops are imaged within one micrograph using a single tilting condition, which also has the benefits of sharp imaging contrast and improved signal-to-noise ratio compared to CTEM, shown in Figures 9b-e.

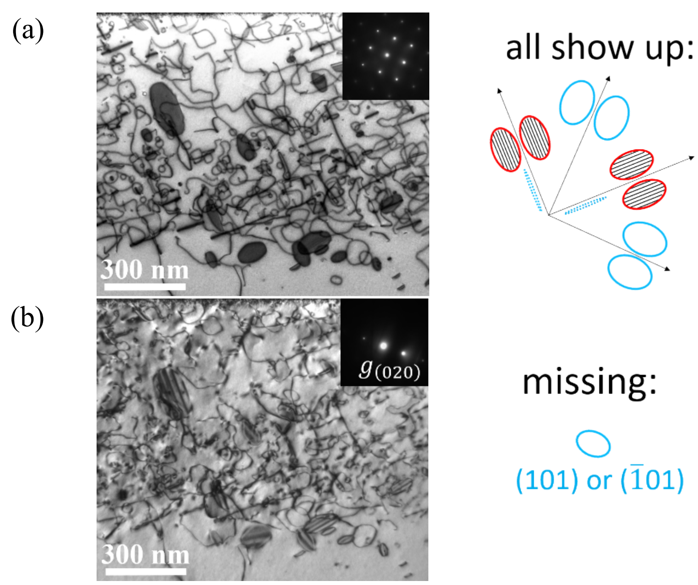

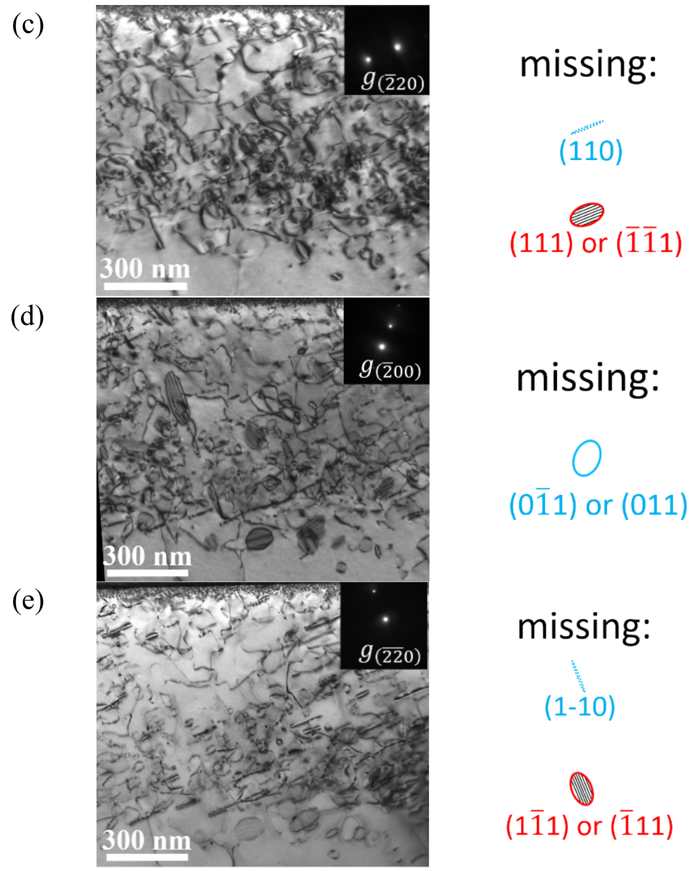

Figure 9. Correlated (a) on-zone [001] *STEM-BF, and multiple CTEM-BF kinematical two-beam condition images near* [001] *zone axis using multiple* ***g*** *vectors of (b)* (020)*, (c)* $(\bar{2}20)$*, (d)* $(\bar{2}00)$*, and (e)* $(\bar{2}\bar{2}0)$*. Note that the missing dislocation loop(s) in (b)~(e) due to the* ***g•b*** *invisibility criterion are provided in Table 1, and the complete labeling for all loop variants are shown in Figure 2.*

The amount of work involved during the full Burgers vector analysis using multiple-***g***-vector two-beam condition imaging and invisibility criterion is extremely intensive. On the contrary, the on-zone STEM-BF imaging technique is simplified significantly, with only a single on-zone tilting condition required to enable the exhibition of all dislocation loop types and variants. In addition, the shadow contrast is very pronounced in [001] on-zone STEM-BF with much improved signal-to-noise ratio as compared to the CTEM two-beam condition images, making it easier to identify the faulted loops using the proposed STEM method.

3.4 CTEM-DF Rel-Rod Imaging

Figure 10 presents the correlated on-zone [011] STEM-BF and the Rel-Rod CTEM-DF where $\boldsymbol{g}_{\bar{3}1\bar{1}}$ and $\boldsymbol{g}_{\bar{3}\bar{1}\bar{1}}$ vectors near [011] zone are used for imaging two faulted loop variants of a/3($\bar{1}\bar{1}$1) and a/3(1$\bar{1}$1) that are nearly edge-on, respectively. As can be seen, the on-zone [011] STEM-BF image in Figure 10 (a) is consistent with the CTEM-DF Rel-Rod method in Figures 10 (b) and (c) for imaging two edge-on variants of faulted dislocation loops.

However, neither the other two inclined variants of faulted loops, nor any perfect loops can be imaged using the Rel-Rod method, while it can be seen in Figure 10 (a) that a significant fraction of dislocation loops in the irradiated microstructure are of the perfect family. Additionally, faulted loop anisotropy is clearly observed: the quantities (i) of the sum of the two inclined variants of a/3(111) and a/3($\bar{1}$11) faulted loops, (ii) of one nearly edge-on variant of a/3($\bar{1}\bar{1}$1) faulted loops, and (iii) of the other nearly edge-on variant of a/3(1$\bar{1}$1) faulted loops can be counted within the area of interest from Figures 10 (a), (b) and (c) as 14, 12 and 13, respectively. In this system and region of interest, the faulted loops tend to preferentially nucleate on the ($\bar{1}\bar{1}$1) and (1$\bar{1}$1) planes over the (111) or ($\bar{1}$11) planes, and this observation might be attributed to the momentum carried by the incident ions that cause the cascade and displacement. This hypothesis needs more detailed studies to verify, and the loop anisotropy is not the scope of the current study.

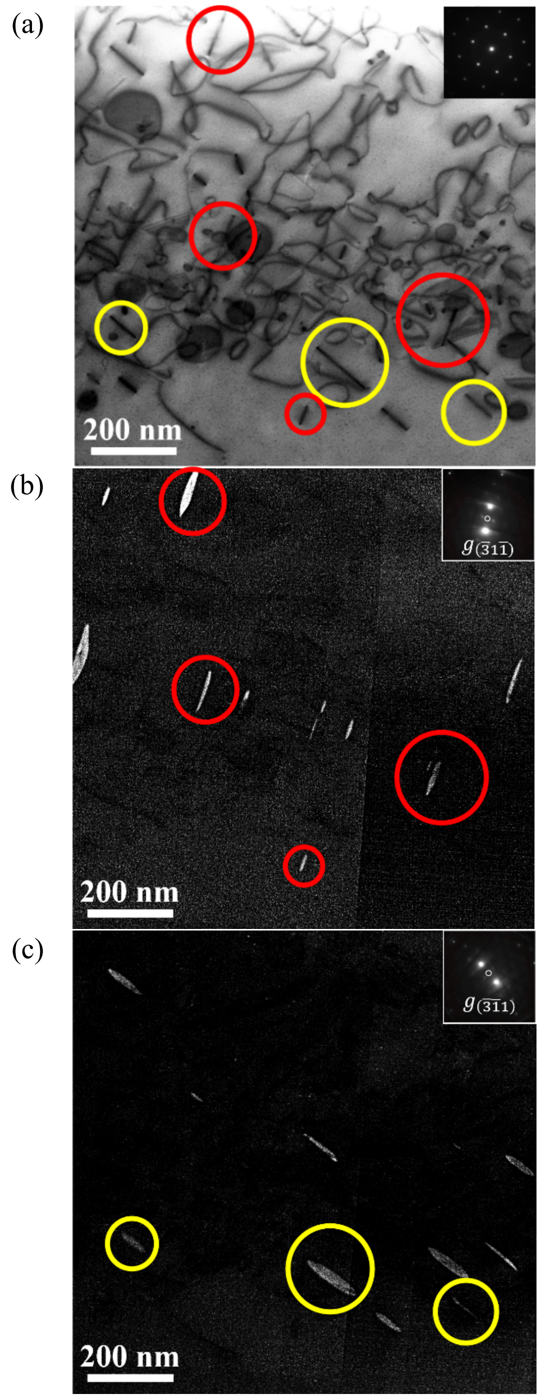

Figure 10. Correlated (a) on-zone [011] *STEM-BF, and Rel-Rod CTEM-DF using (b)* $\boldsymbol{g}_{\bar{3}1\bar{1}}$ *and (c)* $\boldsymbol{g}_{\bar{3}\bar{1}\bar{1}}$ *for imaging* a/3($\bar{1}\bar{1}$1) *and* a/3(1$\bar{1}$1) *faulted loops respectively. The slight tilting of the nearly edge-on faulted loops near the* [011] *zone axis allows for the illumination of the contrast because of the inserted stacking fault plane. Note that the white circles in the diffraction pattern in (b) and (c) denote the position of the inserted objective aperture to obtain the Rel-Rod DF images.*

In summary, although the Rel-Rod technique has the advantage of moderately convenient sample tilting and the capability of capturing high density of the edge-on faulted loops with good sensitivity, the serious shortcomings have been demonstrated here when one tries to understand the full picture of loop evolution involving the necessary imaging of perfect loops, non-edge-on faulted loops, and dislocation lines in FCC materials under irradiation. The on-zone STEM-BF method would allow the observation and identification of both families of loops with all variants using the correlated diffraction pattern, in addition to the advantage of the convenience from a single tilting condition required. Nevertheless, all the techniques demonstrated are effectively coupled and complementary, and thus together provide a toolbox for the nuclear materials microscopists. Due to the ease of use and interpretation of the developed on-zone STEM-BF method at [001] zone axis in this work, this technique is likely to be the first "tool" that should be used for imaging radiation induced dislocation loops in FCC materials.

4. Conclusion

On-zone STEM-based imaging has emerged as an efficient and effective technique for imaging dislocation loops in BCC-based alloys. Here, the technique has been extended to FCC material systems with the optimal imaging conditions identified as on-zone [001] STEM-BF imaging coupled with simultaneous STEM-ADF imaging. Under this imaging condition, not only the signal-to-noise ratio is improved, but more importantly, all four faulted loop variants are inclined in the foil and can be identified by their shadow contrast generated in STEM-BF. STEM-ADF can serve as an additional check during feature overlapping and thus improve the counting precision. On-zone [111] should be avoided without two-beam tilting conditions to confirm loop family or type, because of the lack of shadow contrast for the in-plane faulted loop in the STEM-BF image. The loop morphology obtained using CTEM-BF is the same as STEM-BF, while the dislocation loop core strain field of CTEM-BF image is greater and the shadow contrast of faulted loops are reduced, which hinders accurate identification of loop type and the measurement of loop size. On-zone STEM-BF has also been confirmed to be an accurate tool to identify faulted loops at [011] zone by comparing to the CTEM dark-field Rel-Rod imaging without the assumption of equal fraction of faulted loop variants. Therefore, on-zone [001] STEM-BF imaging is advised as the preferred methodology for dislocation loop imaging in irradiated FCC-based materials.

Acknowledgements

Materials synthesis, ion irradiations, and preliminary characterization of irradiated material was supported as part of the Energy Dissipation to Defect Evolution (EDDE) Center, an Energy Frontier Research Center funded by the US Department of Energy, Office of Science, Basic Energy Sciences under contract number DE-AC05-00OR22725. Detailed characterization and manuscript preparation were supported by the Advanced Fuels Campaign - Nuclear Technology Research and Development program by the US Department of Energy, Office of Nuclear Energy under sub-contract 4000175183 through Oak Ridge National Laboratory. Ion beam work was performed at the UT ORNL Ion Beam Materials Laboratory located on the campus of the University of Tennessee-Knoxville. FIB and S/TEM analysis were conducted in the Michigan Center for Material Characterization of the University of Michigan-Ann Arbor.

Pengyuan Xiu would like to appreciate Dr. Gihan Velisa for performing the ion radiation. Pengyuan Xiu would also like to acknowledge the helpful discussions of various S/C-TEM imaging techniques with: Dr. Kai Sun, Dr. Miao Song, Dr. Tao Ma and Dr. Robert Hovden at University of Michigan; Dr. Kelvin Xie at Texas A&M University; Dr. Lingfeng He and Dr. Jian Gan at Idaho National Laboratory; and Dr. Patrick J Phillips at JEOL USA.

References

[1] T. Diaz De La Rubla, H.M. Zblb, T.A. Khralshl, B.D. Wirth, M. Victoria, M.J. Caturia, Multiscale modelling of plastic flow localization in irradiated materials, Nature. (2000). https://doi.org/10.1038/35022544.

[2] D.J. Edwards, E.P. Simonen, F.A. Garner, L.R. Greenwood, B.M. Oliver, S.M. Bruemmer, Influence of irradiation temperature and dose gradients on the microstructural evolution in neutron-irradiated 316SS, J. Nucl. Mater. (2003). https://doi.org/10.1016/S0022-3115(03)00003-5.

[3] P.G. Tipping, Understanding and mitigating ageing in nuclear power plants, Woodhead Publishing Limited, 2010. https://doi.org/10.1533/9781845699956.

[4] D. Rodney, Molecular dynamics simulation of screw dislocations interacting with interstitial frank loops in a model FCC crystal, Acta Mater. (2004). https://doi.org/10.1016/j.actamat.2003.09.044.

[5] T. Nogaret, C. Robertson, D. Rodney, Atomic-scale plasticity in the presence of Frank loops, Philos. Mag. (2007). https://doi.org/10.1080/14786430601011497.

[6] D.J. Bacon, Y.N. Osetsky, D. Rodney, Chapter 88 Dislocation–Obstacle Interactions at the Atomic Level, in: Dislocations in Solids, Elsevier, 2009: pp. 1–90. https://doi.org/10.1016/S1572-4859(09)01501-0.

[7] L.M. Clarebrough, R.L. Segall, M.H. Loretto, Faulted defects in quenched copper and silver, Philos. Mag. (1966). https://doi.org/10.1080/14786436608213542.

[8] M.L. Jenkins, H. Fukushima, M.A. Kirk, On the determination of loop nature in the TEM, in: Mater. Res. Soc. Symp. - Proc., 1997.

[9] R.M.J. Cotterill, R.L. Segall, The effect of quenching history, quenching temperature and trace impurities on vacancy clusters in aluminium and gold, Philos. Mag. (1963). https://doi.org/10.1080/14786436308207339.

[10] P.S. Dobson, P.J. Goodhew, R.E. Smallman, Climb kinetics of dislocation loops in aluminium, Philos. Mag. (1967). https://doi.org/10.1080/14786436708229253.

[11] W.J. Yang, R.A. Dodd, G.L. Kulcinski, Electron irradiation damage in high purity aluminum, J. Nucl. Mater. (1977). https://doi.org/10.1016/0022-3115(77)90019-8.

[12] Q. Chen, I. Mukouda, Y. Shimomura, Formation of voids and faulted loops in quenched pure aluminum and aluminum dilute (Cu,Si,Mg) alloys, Bull. Fac. Eng. Hiroshima Univ.

Fac. Eng. Hiroshima Univ. (1998).

[13] Y. Satoh, T. Yoshiie, H. Mori, M. Kiritani, Formation of stacking-fault tetrahedra in aluminum irradiated with high-energy particles at low-temperatures, Phys. Rev. B - Condens. Matter Mater. Phys. (2004). https://doi.org/10.1103/PhysRevB.69.094108.

[14] S.B. Fisher, Electron radiation damage in copper in the high voltage electron microscope, Radiat. Eff. 7 (1971) 173–177. https://doi.org/10.1080/00337577108230985.

[15] A.Y. Stathopoulos, C.A. English, B.L. Eyre, P.B. Hirsch, The effect of alloying additions on collision cascades in heavy-ion irradiated copper solid solutions, Philos. Mag. A Phys. Condens. Matter, Struct. Defects Mech. Prop. (1981). https://doi.org/10.1080/01418618108239535.

[16] H.R. Brager, J.L. Straalsund, Defect development in neutron irradiated type 316 stainless steel, J. Nucl. Mater. (1973). https://doi.org/10.1016/0022-3115(73)90131-1.

[17] N. Hashimoto, E. Wakai, J.P. Robertson, Relationship between hardening and damage structure in austenitic stainless steel 316LN irradiated at low temperature in the HFIR, J. Nucl. Mater. (1999). https://doi.org/10.1016/S0022-3115(99)00009-4.

[18] N. Hashimoto, S.J. Zinkle, A.F. Rowcliffe, J.P. Robertson, S. Jitsukawa, Deformation mechanisms in 316 stainless steel irradiated at 60 °C and 330 °C, J. Nucl. Mater. (2000). https://doi.org/10.1016/S0022-3115(00)00087-8.

[19] Z. Jiao, J.T. Busby, G.S. Was, Deformation microstructure of proton-irradiated stainless steels, J. Nucl. Mater. (2007). https://doi.org/10.1016/j.jnucmat.2006.12.012.

[20] M.N. Gussev, K.G. Field, J.T. Busby, Deformation localization and dislocation channel dynamics in neutron-irradiated austenitic stainless steels, J. Nucl. Mater. (2015). https://doi.org/10.1016/j.jnucmat.2015.02.008.

[21] K.G. Field, Y. Yang, T.R. Allen, J.T. Busby, Defect sink characteristics of specific grain boundary types in 304 stainless steels under high dose neutron environments, Acta Mater. (2015). https://doi.org/10.1016/j.actamat.2015.01.064.

[22] X. Liu, J.G. Gigax, J.D. Poplawsky, W. Guo, H. Kim, L. Shao, F.A. Garner, J.F. Stubbins, Radiation response of a Fe–20Cr–25Ni austenitic stainless steel under Fe2+ irradiation at 500 °C, Materialia. (2020). https://doi.org/10.1016/j.mtla.2019.100542.

[23] D.J. Mazey, J.A. Hudson, Observation of large faulted interstitial loops in proton-irradiated nickel, J. Nucl. Mater. (1970). https://doi.org/10.1016/0022-3115(70)90177-7.

[24] D.I.R. Norris, Dislocation loop growth in an electron irradiated thin foil, Philos. Mag. (1970). https://doi.org/10.1080/14786437008226935.

[25] S.A. Briggs, C.M. Barr, J. Pakarinen, M. Mamivand, K. Hattar, D.D. Morgan, M. Taheri, K. Sridharan, Observations of defect structure evolution in proton and Ni ion irradiated Ni-Cr binary alloys, J. Nucl. Mater. (2016). https://doi.org/10.1016/j.jnucmat.2016.06.046.

[26] C. Lu, T. Yang, L. Niu, Q. Peng, K. Jin, M.L. Crespillo, G. Velisa, H. Xue, F. Zhang, P.

Xiu, Y. Zhang, F. Gao, H. Bei, W.J. Weber, L. Wang, Interstitial migration behavior and defect evolution in ion irradiated pure nickel and Ni-xFe binary alloys, J. Nucl. Mater. (2018). https://doi.org/10.1016/j.jnucmat.2018.07.006.

[27] T. ni Yang, C. Lu, G. Velisa, K. Jin, P. Xiu, M.L. Crespillo, Y. Zhang, H. Bei, L. Wang, Effect of alloying elements on defect evolution in Ni-20X binary alloys, Acta Mater. (2018). https://doi.org/10.1016/j.actamat.2018.03.054.

[28] M. Song, C.R. Lear, C.M. Parish, M. Wang, G.S. Was, Radiation tolerance of commercial and advanced alloys for core internals: a comprehensive microstructural characterization, J. Nucl. Mater. (2018). https://doi.org/10.1016/j.jnucmat.2018.08.035.

[29] K. Ma, B. Décamps, A. Fraczkiewicz, F. Prima, M. Loyer-Prost, Drastic influence of micro-alloying on Frank loop nature in Ni and Ni-based model alloys, Mater. Res. Lett. (2020). https://doi.org/10.1080/21663831.2020.1741042.

[30] L.J. Chen, A.J. Ardell, The observation of multiple-layer loops in nickel base alloys under ion bombardment, Phys. Status Solidi. (1976). https://doi.org/10.1002/pssa.2210340232.

[31] H. Ro, T.E. Mitchell, Effects of electron irradiation on precipitation in Ni-Al alloys, Metall. Trans. A. 9 (1978) 1749–1760. https://doi.org/10.1007/BF02663404.

[32] K. Hamada, S. Kojima, Y. Ogasawara, T. Yoshiie, M. Kiritani, Role of solute atoms on microstructural evolution in neutron irradiated nickel, J. Nucl. Mater. (1994). https://doi.org/10.1016/0022-3115(94)90070-1.

[33] B.H. Sencer, G.M. Bond, F.A. Garner, M.L. Hamilton, B.M. Oliver, L.E. Thomas, S.A. Maloy, W.F. Sommer, M.R. James, P.D. Ferguson, Microstructural evolution of Alloy 718 at high helium and hydrogen generation rates during irradiation with 600-800 MeV protons, J. Nucl. Mater. (2000). https://doi.org/10.1016/S0022-3115(00)00308-1.

[34] N. Hashimoto, J.D. Hunn, T.S. Byun, L.K. Mansur, Microstructural analysis of ion-irradiation-induced hardening in inconel 718, in: J. Nucl. Mater., 2003. https://doi.org/10.1016/S0022-3115(03)00013-8.

[35] S.I. Porollo, A.M. Dvoriashin, Y. V. Konobeev, F.A. Garner, Microstructure and swelling of neutron irradiated nickel and binary nickel alloys, J. Nucl. Mater. (2013). https://doi.org/10.1016/j.jnucmat.2013.05.019.

[36] H.K. Zhang, Z. Yao, C. Judge, M. Griffiths, Microstructural evolution of CANDU spacer material Inconel X-750 under in situ ion irradiation, J. Nucl. Mater. (2013). https://doi.org/10.1016/j.jnucmat.2013.06.034.

[37] H.K. Zhang, Z. Yao, G. Morin, M. Griffiths, TEM characterization of in-reactor neutron irradiated CANDU spacer material Inconel X-750, J. Nucl. Mater. (2014). https://doi.org/10.1016/j.jnucmat.2014.03.043.

[38] M.R. He, S. Wang, K. Jin, H. Bei, K. Yasuda, S. Matsumura, K. Higashida, I.M. Robertson, Enhanced damage resistance and novel defect structure of CrFeCoNi under in situ electron irradiation, Scr. Mater. (2016). https://doi.org/10.1016/j.scriptamat.2016.07.023.

[39] C. Lu, T. Yang, K. Jin, N. Gao, P. Xiu, Y. Zhang, F. Gao, H. Bei, W.J. Weber, K. Sun, Y. Dong, L. Wang, Radiation-induced segregation on defect clusters in single-phase concentrated solid-solution alloys, Acta Mater. (2017). https://doi.org/10.1016/j.actamat.2017.01.019.

[40] S. Shi, M.R. He, K. Jin, H. Bei, I.M. Robertson, Evolution of ion damage at 773K in Ni-containing concentrated solid-solution alloys, J. Nucl. Mater. (2018). https://doi.org/10.1016/j.jnucmat.2018.01.015.

[41] D. Chen, Y. Tong, J. Wang, B. Han, Y.L. Zhao, F. He, J.J. Kai, Microstructural response of He+ irradiated FeCoNiCrTi0.2 high-entropy alloy, J. Nucl. Mater. (2018). https://doi.org/10.1016/j.jnucmat.2018.08.006.

[42] C. Lu, T.N. Yang, K. Jin, G. Velisa, P. Xiu, Q. Peng, F. Gao, Y. Zhang, H. Bei, W.J. Weber, L. Wang, Irradiation effects of medium-entropy alloy NiCoCr with and without pre-indentation, J. Nucl. Mater. (2019). https://doi.org/10.1016/j.jnucmat.2019.06.020.

[43] P. Xiu, Y.N. Osetsky, L. Jiang, G. Velisa, Y. Tong, H. Bei, W.J. Weber, Y. Zhang, L. Wang, Dislocation loop evolution and radiation hardening in nickel-based concentrated solid solution alloys, J. Nucl. Mater. 538 (2020) 152247. https://doi.org/10.1016/j.jnucmat.2020.152247.

[44] T. Yang, W. Guo, J.D. Poplawsky, D. Li, L. Wang, Y. Li, W. Hu, M.L. Crespillo, Z. Yan, Y. Zhang, Y. Wang, S.J. Zinkle, Structural damage and phase stability of Al0.3CoCrFeNi high entropy alloy under high temperature ion irradiation, Acta Mater. (2020). https://doi.org/10.1016/j.actamat.2020.01.060.

[45] Y.N. Osetsky, F. Gao, D.J. Bacon, Glissile and sessile vacancy and self-interstitial clusters in BCC and FCC metals, Mater. Res. Soc. Symp. - Proc. (1999). https://doi.org/10.1557/proc-540-691.

[46] Y.N. Osetsky, D.J. Bacon, A. Serra, B.N. Singh, S.I. Golubov, Stability and mobility of defect clusters and dislocation loops in metals, J. Nucl. Mater. (2000). https://doi.org/10.1016/S0022-3115(99)00170-1.

[47] D.J. Edwards, E.P. Simonen, S.M. Bruemmer, Evolution of fine-scale defects in stainless steels neutron-irradiated at 275 °C, J. Nucl. Mater. (2003). https://doi.org/10.1016/S0022-3115(03)00002-3.

[48] L. Tan, J.T. Busby, H.J.M. Chichester, K. Sridharan, T.R. Allen, Thermomechanical treatment for improved neutron irradiation resistance of austenitic alloy (Fe-21Cr-32Ni), J. Nucl. Mater. (2013). https://doi.org/10.1016/j.jnucmat.2013.01.333.

[49] F.A. Garner, D.S. Gelles, Irradiation creep mechanisms: An experimental perspective, J. Nucl. Mater. (1988). https://doi.org/10.1016/0022-3115(88)90098-0.

[50] C.B. Carter, D.B. Williams, Transmission electron microscopy: Diffraction, imaging, and spectrometry, 2016. https://doi.org/10.1007/978-3-319-26651-0.

[51] B. Yao, D.J. Edwards, R.J. Kurtz, TEM characterization of dislocation loops in irradiated bcc Fe-based steels, J. Nucl. Mater. (2013). https://doi.org/10.1016/j.jnucmat.2012.12.002.

[52] C.M. Parish, K.G. Field, A.G. Certain, J.P. Wharry, Application of STEM characterization for investigating radiation effects in BCC Fe-based alloys, J. Mater. Res. (2015). https://doi.org/10.1557/jmr.2015.32.

[53] J.E. Nathaniel, A.C. Lang, O. El-Atwani, P.K. Suri, J.K. Baldwin, M.A. Kirk, Y. Wang, M.L. Taheri, Toward high-throughput defect density quantification: A comparison of techniques for irradiated samples, Ultramicroscopy. (2019). https://doi.org/10.1016/j.ultramic.2019.112820.

[54] Y. Zhu, C. Ophus, M.B. Toloczko, D.J. Edwards, Towards bend-contour-free dislocation imaging via diffraction contrast STEM, Ultramicroscopy. (2018). https://doi.org/10.1016/j.ultramic.2018.06.001.

[55] Y. Miyajima, M. Mitsuhara, S. Hata, H. Nakashima, N. Tsuji, Quantification of internal dislocation density using scanning transmission electron microscopy in ultrafine grained pure aluminium fabricated by severe plastic deformation, Mater. Sci. Eng. A. (2010). https://doi.org/10.1016/j.msea.2010.09.058.

[56] P.J. Phillips, M.C. Brandes, M.J. Mills, M. de Graef, Diffraction contrast STEM of dislocations: Imaging and simulations, Ultramicroscopy. (2011). https://doi.org/10.1016/j.ultramic.2011.07.001.

[57] R.J. Arsenault, M.S. of A.N.M. Committee., U.S.N.B. of Standards., N.S.F. (U.S.), Defects and Defect Clusters in B.c.c. Metals and Their Alloys: Proceedings, National Bureau of Standards, 1973.

[58] C. Lu, L. Niu, N. Chen, K. Jin, T. Yang, P. Xiu, Y. Zhang, F. Gao, H. Bei, S. Shi, M.R. He, I.M. Robertson, W.J. Weber, L. Wang, Enhancing radiation tolerance by controlling defect mobility and migration pathways in multicomponent single-phase alloys, Nat. Commun. (2016). https://doi.org/10.1038/ncomms13564.

[59] K. Jin, C. Lu, L.M. Wang, J. Qu, W.J. Weber, Y. Zhang, H. Bei, Effects of compositional complexity on the ion-irradiation induced swelling and hardening in Ni-containing equiatomic alloys, Scr. Mater. (2016). https://doi.org/10.1016/j.scriptamat.2016.03.030.

[60] C. Lu, T. Yang, K. Jin, G. Velisa, P. Xiu, M. Song, Q. Peng, F. Gao, Y. Zhang, H. Bei, W.J. Weber, L. Wang, Enhanced void swelling in NiCoFeCrPd high-entropy alloy by indentation-induced dislocations, Mater. Res. Lett. (2018). https://doi.org/10.1080/21663831.2018.1504136.

[61] Y. Zhang, X. Wang, Y.N. Osetsky, Y. Tong, R. Harrison, S.E. Donnelly, D. Chen, Y. Wang, H. Bei, B.C. Sales, K.L. More, P. Xiu, L. Wang, W.J. Weber, Effects of 3d electron configurations on helium bubble formation and void swelling in concentrated solid-solution alloys, Acta Mater. (2019). https://doi.org/10.1016/j.actamat.2019.10.013.

[62] T. ni Yang, C. Lu, G. Velisa, K. Jin, P. Xiu, Y. Zhang, H. Bei, L. Wang, Influence of irradiation temperature on void swelling in NiCoFeCrMn and NiCoFeCrPd, Scr. Mater. (2019). https://doi.org/10.1016/j.scriptamat.2018.08.021.

[63] Y. Zhang, M.L. Crespillo, H. Xue, K. Jin, C.H. Chen, C.L. Fontana, J.T. Graham, W.J. Weber, New ion beam materials laboratory for materials modification and irradiation

effects research, Nucl. Instruments Methods Phys. Res. Sect. B Beam Interact. with Mater. Atoms. (2014). https://doi.org/10.1016/j.nimb.2014.07.028.

[64] J.F. Ziegler, J.P. Biersack, The Stopping and Range of Ions in Matter, in: Treatise Heavy-Ion Sci., 1985. https://doi.org/10.1007/978-1-4615-8103-1_3.

[65] J.F. Ziegler, M.D. Ziegler, J.P. Biersack, SRIM - The stopping and range of ions in matter (2010), Nucl. Instruments Methods Phys. Res. Sect. B Beam Interact. with Mater. Atoms. (2010). https://doi.org/10.1016/j.nimb.2010.02.091.

[66] W.J. Weber, Y. Zhang, Predicting damage production in monoatomic and multi-elemental targets using stopping and range of ions in matter code: Challenges and recommendations, Curr. Opin. Solid State Mater. Sci. (2019). https://doi.org/10.1016/j.cossms.2019.06.001.

[67] A. Schemer-Kohrn, M.B. Toloczko, Y. Zhu, J. Wang, D.J. Edwards, Removal of FIB Damage using Flash Electropolishing for Artifact-free TEM Foils, Microsc. Microanal. (2019). https://doi.org/10.1017/s1431927619008766.

[68] P.J. Phillips, M.J. Mills, M. De Graef, Systematic row and zone axis STEM defect image simulations, Philos. Mag. (2011). https://doi.org/10.1080/14786435.2010.547526.

[69] M.J. Whelan, P.B. Hirsch, Electron diffraction from crystals containing stacking faults: II, Philos. Mag. (1957). https://doi.org/10.1080/14786435708243208.

[70] R.E. Smallman, A.H.W. Ngan, Modern Physical Metallurgy: Eighth Edition, 2013. https://doi.org/10.1016/C2011-0-05565-5.

[71] P.J. Maziasz, Overview of microstructural evolution in neutron-irradiated austenitic stainless steels, J. Nucl. Mater. (1993). https://doi.org/10.1016/0022-3115(93)90077-C.

[72] S.J. Zinkle, P.J. Maziasz, R.E. Stoller, Dose dependence of the microstructural evolution in neutron-irradiated austenitic stainless steel, J. Nucl. Mater. (1993). https://doi.org/10.1016/0022-3115(93)90128-L.

[73] D. Hull, D.J. Bacon, Introduction to Dislocations, 2011. https://doi.org/10.1016/C2009-0-64358-0.

[74] M.J. Whelan, P.B. Hirsch, Electron diffraction from crystals containing stacking faults: I, Philos. Mag. (1957). https://doi.org/10.1080/14786435708242742.

[75] D.M. Maher, D.C. Joy, The formation and interpretation of defect images from crystalline materials in a scanning transmission electron microscope, Ultramicroscopy. (1976). https://doi.org/10.1016/0304-3991(76)90038-3.

[76] E.H. Lee, L.K. Mansur, M.H. Yoo, Spatial variation in void volume during charged particle bombardment - the effects of injected interstitials, J. Nucl. Mater. (1979). https://doi.org/10.1016/0022-3115(79)90548-8.

[77] F.A. Garner, Impact of the injected interstitial on the correlation of charged particle and neutron-induced radiation damage, J. Nucl. Mater. (1983). https://doi.org/10.1016/0022-3115(83)90023-5.

[78] M.P. Short, D.R. Gaston, M. Jin, L. Shao, F.A. Garner, Modeling injected interstitial

effects on void swelling in self-ion irradiation experiments, J. Nucl. Mater. (2016). https://doi.org/10.1016/j.jnucmat.2015.10.002.

[79] T. ni Yang, C. Lu, K. Jin, M.L. Crespillo, Y. Zhang, H. Bei, L. Wang, The effect of injected interstitials on void formation in self-ion irradiated nickel containing concentrated solid solution alloys, J. Nucl. Mater. (2017). https://doi.org/10.1016/j.jnucmat.2017.02.026.

[80] P. Rez, A transport equation theory of beam spreading in the electron microscope, Ultramicroscopy. (1983). https://doi.org/10.1016/0304-3991(83)90302-9.

[81] J.P. Tartour, J. Washburn, Climb kinetics of dislocation loops in aluminium, Philos. Mag. 18 (1968) 1257–1267. https://doi.org/10.1080/14786436808227755.

[82] E. Levo, F. Granberg, C. Fridlund, K. Nordlund, F. Djurabekova, Radiation damage buildup and dislocation evolution in Ni and equiatomic multicomponent Ni-based alloys, J. Nucl. Mater. (2017). https://doi.org/10.1016/j.jnucmat.2017.04.023.

[83] L. Tan, J.T. Busby, Formulating the strength factor α for improved predictability of radiation hardening, J. Nucl. Mater. (2015). https://doi.org/10.1016/j.jnucmat.2015.07.009.

[84] G.S. Was, Fundamentals of radiation materials science: Metals and alloys, second edition, 2016. https://doi.org/10.1007/978-1-4939-3438-6.

[85] N.S. Husseini, D.P. Kumah, J.Z. Yi, C.J. Torbet, D.A. Arms, E.M. Dufresne, T.M. Pollock, J. Wayne Jones, R. Clarke, Mapping single-crystal dendritic microstructure and defects in nickel-base superalloys with synchrotron radiation, Acta Mater. (2008). https://doi.org/10.1016/j.actamat.2008.05.041.

[86] J.M. Rosalie, C. Dwyer, L. Bourgeois, On chemical order and interfacial segregation in <mml:math altimg="si24.gif" overflow="scroll" xmlns:xocs="http://www.elsevier.com/xml/xocs/dtd" xmlns:xs="http://www.w3.org/2001/XMLSchema" xmlns:xsi="http://www.w3.org/2001/XMLSchema-instance" xmlns="http:, Acta Mater. (2014). https://doi.org/10.1016/j.actamat.2014.01.032.

[87] W. Li, K.G. Field, D. Morgan, Automated defect analysis in electron microscopic images, Npj Comput. Mater. (2018). https://doi.org/10.1038/s41524-018-0093-8.

[88] C.M. Anderson, J. Klein, H. Rajakumar, C.D. Judge, L.K. B, Automated Detection of Helium Bubbles in Irradiated X-750, Ultramicroscopy. (2020). https://doi.org/10.1016/j.ultramic.2020.113068.